TU Delft

Delft University of Technology

Hydrodynamics of expanded bed adsorption studied through CFD-DEM

Nijssen, Tim M.J.; Padding, Johan T.; Ottens, Marcel

DOI
10.1016/j.ces.2023.119027

Publication date
2023

Document Version
Final published version

Published in
Chemical Engineering Science

Citation (APA)
Nijssen, T. M. J., Padding, J. T., & Ottens, M. (2023). Hydrodynamics of expanded bed adsorption studied through CFD-DEM. *Chemical Engineering Science*, *280*, Article 119027. https://doi.org/10.1016/j.ces.2023.119027

Important note
To cite this publication, please use the final published version (if applicable).
Please check the document version above.

Copyright
Other than for strictly personal use, it is not permitted to download, forward or distribute the text or part of it, without the consent of the author(s) and/or copyright holder(s), unless the work is under an open content license such as Creative Commons.

Takedown policy
Please contact us and provide details if you believe this document breaches copyrights.
We will remove access to the work immediately and investigate your claim.

This work is downloaded from Delft University of Technology.
For technical reasons the number of authors shown on this cover page is limited to a maximum of 10.

Chemical Engineering Science 280 (2023) 119027

Contents lists available at ScienceDirect

Chemical Engineering Science

journal homepage: www.elsevier.com/locate/ces

Hydrodynamics of expanded bed adsorption studied through CFD-DEM

Tim M.J. Nijssen [a,b,*], Johan T. Padding [b], Marcel Ottens [a]

[a] Delft University of Technology, Department of Biotechnology. Van der Maasweg 9, 2629 HZ, Delft, the Netherlands
[b] Delft University of Technology, Faculty of Mechanical, Maritime and Materials Engineering, Department of Process & Energy. Leeghwaterstraat 39, 2628 CB, Delft, the Netherlands

ARTICLE INFO

Keywords:
Expanded bed adsorption
Hydrodynamics
Liquid-solid fluidisation
Computational fluid dynamics
Discrete element method

ABSTRACT

The hydrodynamics of the Expanded Bed Adsorption process is studied through simulations combining Computational Fluid Dynamics and the Discrete Element Method. A representative base case is defined, based on process design parameters commonly encountered in literature. Then, 19 other cases are defined, each representing a singular adjustment to the column design, material properties, or operating conditions. The parameters that are varied are the expansion factor, liquid viscosity, bed aspect ratio, mean particle density, width of the particle density distribution, width of the particle size distribution, column taper angle, and column alignment angle. The impact of each adjustment on the bed behaviour is discussed, using the local particle size distribution and solids dispersion coefficient as main indicators of bed stability. Optimal performance was found for an expansion factor of two to three, and the combination of particle size distribution and particle density distribution was found to greatly improve bed stability. The mixing process of the liquid and solid phases is concluded to be of highly complex nature, and cannot simply be predicted from the liquid flow velocity.

1. Introduction

The purification of biopharmaceutical products represents a major part of their manufacturing process. Up to 80% of the total production costs is associated with the downstream processing of the fermentation broth (D'Souza et al., 2013). The purification process typically consists of many consecutive separation steps. These are needed to isolate the target molecule from the complex mixture of proteins and cell parts, and obtain the high purity required for clinical application. In the 1990s, Expanded Bed Adsorption (EBA) was introduced as a means of process intensification in this purification train (Hjorth, 1997).

In the traditional downstream process, the fermentation broth is first clarified. Then, through centrifugation, microfiltration, or a combination thereof all cells and cell parts are removed from the mixture. This clarified feedstock can then be applied to a series of packed bed chromatography columns, in which the target molecule is captured and further purified by adsorption to the bed of resin beads. Lastly, formulation steps prepare the product for packaging and shipping (D'Souza et al., 2013).

Expanded Bed Adsorption was developed with the aim to combine the clarification and capture steps into a single unit operation. By performing the initial chromatography step in a mildly fluidised (i.e. expanded) bed, rather than a packed bed, the need for clarification is mitigated. Any particulates or cell material which would clog a packed bed pass freely through the expanded bed, while the target molecule adsorbs to the resin particles. The product is reclaimed in an elution step, and washing and regeneration steps prepare the bed for the next cycle (Lihme et al., 2000)

The advantages of EBA over the traditional process are evident; by elimination of the clarification steps, equipment costs and footprint are diminished. Furthermore, the shorter process reduces product degradation and cuts operation costs (Doeven and den Boer, 2011; D'Souza et al., 2013). However, various practical problems have hindered the large-scale adaptation of the technology, and very few manufacturers have decided to sustain the application of EBA (D'Souza et al., 2013; Jin, 2015). Commonly reported challenges of EBA include:

- Reduced separation efficiency due to mixing of the liquid phase (Jin, 2015)
- Reduced dynamic binding capacity at higher expansions ($H/H_0 \geq 2$) restricting the flow rate (Chang and Chase, 1996; Tong and Sun, 2002a; Lin et al., 2004)
- Limited throughput due to low-density sorbents exhibiting low terminal velocities (Chase and Draeger, 1992a; D'Souza et al., 2013)

* Corresponding author at: Delft University of Technology, Department of Process & Energy. Leeghwaterstraat 39, 2628 CB, Delft, the Netherlands.
E-mail address: t.m.j.nijssen@tudelft.nl (T.M.J. Nijssen).

https://doi.org/10.1016/j.ces.2023.119027
Received 24 March 2023; Received in revised form 1 June 2023; Accepted 20 June 2023
Available online 24 June 2023
0009-2509/© 2023 The Author(s). Published by Elsevier Ltd. This is an open access article under the CC BY license (http://creativecommons.org/licenses/by/4.0/).

- Aggregation and instability in the presence of cells interacting with the resin beads (Lin et al., 2003, 2004; D'Souza et al., 2013)
- Decreased adsorption capacity and rate in the presence of cells (Xia et al., 2007)
- Fouling, clogging and bad hygiene of the flow distributor (Jin, 2015)
- Unstable expansion under high-viscosity conditions, forcing dilution of the feedstock (Chase and Draeger, 1992a)
- High buffer consumption due to the large volume required to obtain stable bed (up to 6 times the settled bed volume) (Lin et al., 2003; Yang and Sun, 2005)
- Low concentration factor due to the high elution volume (Jin, 2015)

These challenges illustrate the need for further research into the promising EBA technology. Specifically, many points connect to the hydrodynamics of the expanded bed and its stability under various conditions. Therefore, in this work we focus on the hydrodynamic behaviour of the EBA column and assess a wide range of operating parameters.

1.1. Previous experimental work

Since its introduction in the 1990s, multiple research groups have focused on the hydrodynamic stability of the EBA column. Their approaches have mainly been experimental, often involving the measurement of residence time distributions, dispersion coefficients, and dynamic binding capacities, all using various sorbents and conditions. A short overview of the main findings is provided below.

Chase and Draeger (1992b) delivered proof of concept for ion exchange adsorption, and found that adsorption could be conducted at up to 4× expansion without significant loss of efficiency. In follow-up work Chase and Draeger (1992a), the authors noted the need for high-density sorbents to achieve sufficient throughput in highly viscous feedstocks (e.g. in presence of nucleic acid polymers). Among others, Pålsson et al. (2000) developed such high-density sorbent particles, allowing for higher stable flow rates.

Chang and Chase (1996) found increased mixing and decreased adsorption capacity with increasing flow rate, liquid viscosity, or expansion. Xia et al. (2007) found the most stable bed configuration is obtained in the range of 2-2.5x expansion. In this range, the loss of adsorption capacity with respect to the packed bed was minimised, around 5%. Ghose and Chase (2000) investigated the influence of the column dimensions. They found the adsorption capacity to be independent of the column diameter, but observed increased mixing at lower bed aspect ratios. Similar effects were observed by Jahanshahi et al. (2009), who found the weakest mixing for a bed aspect ratio of 5.

In an extensive study, Lin et al. (2013) measured axial voidage, particle size, and particle density distributions. They found that, for a lognormal particle size distribution, the local mean particle size, mean particle density and void fraction all follow the same s-shaped curve. In later work Lin et al. (2015), they also measured the liquid dispersion coefficient along the height of the bed. They found a low-mixing zone between 60% and 80% of the total bed height, with increasing mixing towards both the top and bottom. In earlier work, Yun et al. (2004b, 2005) found liquid mixing to be the strongest near the bottom of the bed, decreasing further upwards. These differences were found strongest at lower liquid velocities and higher particle densities.

Tong and Sun (2002b,a) performed measurements on mixing of both the liquid and solid phases. They found that the expanded bed might stratify by particle size or particle density, depending on the width of the respective distributions. Even for a stable size-stratified bed, they observed wide local particle size distributions, indicating the strength of solids mixing. The solids mixing was also investigated by Ewert (2016), who used Positron Emission Particle Tracking (PEPT) to measure the movement of individual sorbent particles within the bed. They found that mobility of the particles is much higher towards the top of the bed. The author reported solids dispersion coefficients, which signify the continual horizontal and vertical fluctuations in particle positions, even in a stable stratified bed.

Whereas many studies focused on the steady-state behaviour of the bed, Lin et al. (2003, 2004) studied the transient behaviour, as well as the influence of cell-sorbent interactions. They found that the addition of interacting cells can strongly destabilise the bed. In some cases stability was not recovered at all, while in others recovery took up to 6 bed volumes of liquid passing through the bed. The authors found that by increasing the ionic strength of the buffer, the electrostatic interactions could be weakened and adverse effects diminished. Similar results were reported by D'Souza et al. (2017), who adjusted the mobile phase composition in an expanded bed with cell presence, and observed improved bed stability by consequence.

1.2. Numerical work

With the increase of widely available computing power came numerical tools for the study of complex systems such as the EBA column. Numerical methods provide numerous advantages over traditional experimental methods. Especially in the field of multiphase flows, experimental techniques (e.g. Particle Image Velocimetry, Positron Emission Particle Tracking, Magnetic Resonance Imaging, etc.) are complicated and sometimes prohibitively expensive, while ultimately providing only limited insight in the flow behaviour. Numerical techniques, on the other hand, often grant full access to the flow domain and yield data which cannot be obtained otherwise.

Another strong advantage of computational research is the freedom of choice in physical parameters. When dealing with real-life materials and equipment, their properties often cannot be tuned independently. The freedom numerical methods offer in this regard allows for the separation of physical phenomena, and can lead to new insights into the underlying physics. It is obvious that the researcher should ensure their simulations remain representative of the real-life system of interest through experimental validation.

A major downside of numerical methods used to be the often lengthy calculations required. However, with the ongoing growth of available High Performance Computing (HPC) facilities, scientists are gaining more and more access to state-of-the-art resources. With the help of such HPC centres, large parametric studies can easily be performed in parallel, and numerical studies are growing increasingly valuable.

The body of numerical work on EBA is considerably smaller than the experimental literature, but various computational methods have been applied throughout the technology's development. Early work focused on mathematical modelling of the concentration profiles along the column height. This goes back to the early 1990s, when Draeger and Chase (1990) used such a model to derive mass transfer properties from their experimental data. A more elaborate mathematical model was developed by Wright and Glasser (2001), who considered dispersion in both the liquid and solid phases. Their work highlighted the importance of mass transfer limitations for the efficacy of the EBA process. Bruce and Chase (2002) combined their model with advanced monitoring of their experimental set-up, working towards real-time model-predictive process control. An entirely different approach was employed by de Araújo Padilha et al. (2017), who used recurrent neural networks to fit chromatograms obtained from an EBA set-up. Unfortunately, such an approach provided little fundamental insight into the governing physics and chemistry of the process.

In more recent years, the increased availability of computing power has paved the way for more in-depth modelling of the hydrodynamics of the EBA column. Koppejan et al. (2018) provided an overview of the available modelling techniques, and demonstrated the value of Computational Fluid Dynamics through a case study on liquid distributor designs. Ren et al. (2021) used Two-Fluid Modelling (TFM) to simulate adsorption processes in liquid-solid fluidised beds. In this approach, the solid phase is represented as a continuum. As the authors demonstrated,

finding the correct models and parameters describing this continuous solid phase is a precarious process, and a source of great uncertainty for the model results. Nevertheless, the authors were able the show the importance of turbulent mass diffusion for the adsorption process.

1.3. Current work

Despite considerable research effort, no systematic study of the column, material and operation parameters governing the performance of the EBA process has been conducted. This knowledge gap can be attributed to the availability and costs of the required equipment and materials, as well the difficulty of performing in-depth measurements in such a complex, multiphase system. In this work, we overcome these challenges by employing a combination of Computational Fluid Dynamics (CFD) and Discrete Element Method (DEM) to study the hydrodynamic behaviour of an EBA column. While computationally expensive, it allows us to freely set material properties without excessive amounts of parameter tuning.

We use this model to perform a parametric study on the hydrodynamic behaviour of a lab-scale EBA column, and to investigate the influence of material properties, column design and operation parameters on the stability and performance of the expanded bed. We assess the expansion of the bed, the liquid flow profile, as well as particle-scale parameters such as local particle size distribution and solids dispersion coefficient. The current work is focused on the hydrodynamics at steady-state. We demonstrate the applicability of the CFD-DEM method and provide a perspective on a future integrated model encompassing mass transfer and adsorption phenomena.

2. Model description

2.1. Model description

In the unresolved CFD-DEM method, systems of interacting continuous (fluid) and discrete (particle) phases are simulated through a coupling of Computational Fluid Dynamics and Discrete Element Method models. In CFD, specifically the Finite Volume method (Versteeg and Malalasekera, 1995) employed here, the simulation domain is divided into control volumes (cells) of volume ΔV, over which discretised mass and momentum balances are solved to resolve the fluid flow. In DEM, particles are treated as individual entities, and their pathways resolved through explicit integration of the laws of motion. The coupling between the continuous and discrete phases is established through evaluation of the interaction force between each particle and its surrounding fluid. The unresolved nature of the method relates to the fact that the CFD cells are larger than the particles, and the interaction force is estimated through models rather than fully resolved.

2.1.1. Governing equations

In the following paragraphs, we provide a short overview of the most important equations governing the method. A detailed description of the mathematical details is beyond the scope of this article. For this, we kindly refer the reader to the works cited below. An in-depth description of the coupling between the solid and liquid phases is provided in Nijssen et al. (2020). In Nijssen et al. (2021), the current model was compared with experimental results and found to predict liquid-solid bed expansion within 10% deviation.

Throughout this article, we use $\vec{u}$ to denote to the fluid velocity, $\vec{v}$ for the particle velocity, $\vec{\Omega}$ for the particle angular velocity, ε for the local fluid volume fraction, and subscripts f and p to refer to the fluid and particle phases, respectively.

The fluid motion is described by the continuity equation (Eq. (1)) and the Navier-Stokes equations (Eq. (2)). The formulation presented here is known as Set II in the work of Zhou et al. (2010). As shown, we have chosen to omit the first term in the continuity equation, which is discussed further in Section 2.2. In these equations, $\vec{\tau} = \mu_f \left[(\nabla \vec{u}) + (\nabla \vec{u})^T \right]$ is the viscous stress tensor and $\vec{F}_{pf} = \sum \vec{f}_{pf} / \Delta V$ is the total particle-fluid momentum exchange in a cell of volume ΔV. The interaction force $\vec{f}_{pf}$ is calculated as the sum of the drag (Di Felice, 1994), lift (Loth, 2008), virtual mass (Felderhof, 1991; Nijssen et al., 2020) and Basset history forces (Parmar et al., 2018; Nijssen et al., 2020) acting on each particle. These models are described in detail in the respective references. While the Di Felice drag model does not explicitly account for polydispersity, the local particle size distribution in our cases of interest is narrow, and the monodisperse model provides a reasonable approximation for the drag force.

$$\cancel{\frac{\partial \varepsilon}{\partial t}} + \nabla \cdot (\varepsilon \vec{u}) = 0 \tag{1}$$

$$\frac{\partial \rho_f \varepsilon \vec{u}}{\partial t} + \nabla \cdot \left(\rho_f \varepsilon \vec{u} \vec{u} \right) = -\varepsilon \nabla p + \varepsilon \nabla \cdot \vec{\tau} + \rho_f \varepsilon \vec{g} - \vec{F}_{pf} \tag{2}$$

The motion of the particles is described by Newton's second law of translational (Eq. (3)) and rotational motion (Eq. (4)). The contact force $\vec{f}_c$ and torque $\vec{T}_c$ resulting from contact with neighbouring particles are prescribed through the Herzian contact model (Di Renzo and Di Maio, 2004). The lubrication force $\vec{f}_l$ is associated with the draining and filling of the thin liquid film between colliding particles. Its calculation was described in-depth in a previous work (Nijssen et al., 2023b). The latter terms in Eq. (3) represent the forces resulting from the pressure gradient, viscous stress gradient, and gravity, respectively. The hydrodynamic torque $\vec{T}_f$ is discussed in Section 2.2.

$$m_p \frac{d\vec{v}}{dt} = \sum_{\text{neigh}} \left(\vec{f}_c + \vec{f}_l \right) + \vec{f}_{pf} + V_p \left[-\nabla p - \nabla \cdot \vec{\tau} + (\rho_p - \rho_f) \vec{g} \right] \tag{3}$$

$$\vec{I} \cdot \frac{d\vec{\Omega}}{dt} = \sum_{\text{neigh}} \left(\vec{T}_c \right) + \vec{T}_f \tag{4}$$

2.2. Numerical stability

The CFD-DEM method was initially mainly applied to gas-solid systems (e.g. Goniva et al., 2012). Its underlying physical concepts also apply to liquid-solid systems. However, the stiffer coupling between the discrete and continuous phases (due to the smaller density difference between them) leads to issues of numerical instability. This is further complicated by the strongly polydisperse system considered in this work. In this section, we present our methods for alleviating the stability issues we encountered during the development of this work.

Firstly, we noticed an accumulation of rotational kinetic energy in the particle phase, leading to erratic particle behaviour. This stemmed from the reduced direct particle-particle friction resulting from normal lubrication forces (Nijssen et al., 2023b), which provided insufficient dissipation of rotational energy. We have resolved this by introducing the hydrodynamic torque or rotational drag, describing the friction between a rotating particle and its surrounding fluid.

The hydrodynamic torque is expressed by Eq. (5) Crowe et al. (2012). The torque coefficient C_T is taken as the maximum of the low-Reynolds limit (Crowe et al., 2012) and the finite-Reynolds model by Dennis et al. (1980), as shown in Eq. (6). Here, we use the rotational Reynolds number $\mathrm{Re}_\Omega = |\vec{\Omega}| d_p^2 / 4\nu_f$. We assume that particle rotation is much stronger than the fluid vorticity, and that the hydrodynamic torque can be implemented with a one-way coupling i.e. the rotational energy is quickly dissipated in the liquid phase and does not influence the fluid flow.

$$\vec{T} = -\frac{\pi}{2} \frac{d_p^5}{32} \rho_f C_T |\vec{\Omega}| \vec{\Omega} \tag{5}$$

$$C_T = \max \left[\frac{16}{\mathrm{Re}_\Omega}; \frac{16}{\mathrm{Re}_\Omega} \left(0.639 + 0.128 \cdot \mathrm{Re}_\Omega^{\frac{1}{2}} \right) \right] \tag{6}$$

A second challenge is presented by the wide particle size distribution employed in EBA processes, which means it is difficult to maintain a constant particle-to-cell-size ratio $d_p / \Delta x$ across the column. It is well

Table 1
Properties and settings describing the base case simulation #1.

Column diameter	D	10	mm	e.g. Jahanshahi et al. (2009)
Column length	L	1.25 H	mm	
Taper angle	α	0.0	deg	
Column alignment	ϑ	0.0	deg	
Aspect ratio	H_0/D	5.0	-	e.g. Jahanshahi et al. (2009)
Expansion	H/H_0^{pred}	2.0	-	e.g. Jahanshahi et al. (2009)
Fluid density	ρ_f	1,000	kg/m^3	
Fluid viscosity	ν_f	10^{-6}	m^2/s	
PSD type	lognormal by volume			e.g. Lin et al. (2013)
PSD range	d_p	100 - 300	μm	e.g. Wu et al. (2018)
PSD mean	$\langle d_p \rangle$	$\sqrt{d_{p,\min} \cdot d_{p,\max}}$	μm	
PSD standard deviation	σ_{dp}	$\left(d_{p,\max}/d_{p,\min}\right)^w$	-	
PSD width	w	1/4	-	e.g. Tong and Sun (2002b)
Mean particle density	$\langle \rho_p \rangle$	1,500	kg/m^3	e.g. Yun et al. (2004a)
Particle density standard deviation	$\sigma_{\rho p}$	0.0	kg/m^3	
Minimum fluidisation velocity	$\lvert\vec{u}_{mf}\rvert$	0.046 - 0.41	mm/s	
Terminal velocity	$\lvert\vec{u}_t\rvert$	2.57 - 16.83	mm/s	
Young's modulus	Y	1.0	MPa	Dorn et al. (2017)
Poisson's ratio	ν_p	0.2	-	Dorn et al. (2017)
Friction coefficient (dry)	$\mu_{f,\text{dry}}$	0.3	-	Keener et al. (2008)
Friction coefficient (lubricated)	$\mu_{f,\text{lub}}$	0.1	-	Keener et al. (2008)
Restitution coefficient	e	0.95	-	Dorn et al. (2017)
Surface roughness	σ	1	μm	Staby et al. (2006)
CFD cell size	Δx	200	μm	Volk et al. (2017)
CFD time step	Δt_{CFD}	$2 \cdot 10^{-4}$	s	
DEM time step	Δt_{DEM}	$5 \cdot 10^{-6}$	s	

known that this ratio is of high importance to the accuracy of the CFD-DEM method (Volk et al., 2017). Mesh-independent results can be achieved by mapping or smoothing algorithms, which enable spreading of the influence of large particles to multiple CFD cells (Sun and Xiao, 2015a,b). Previous results have shown that such algorithms can eliminate artificial heterogeneity in liquid-solid fluidised bed simulations (Esteghamatian et al., 2018). Our tests have shown that mesh-independence is achieved at $\Delta x = 200$ μm, combined with adaptive smoothing of the void fraction and momentum exchange fields. Mesh independence was studied using particle kinetic energy as an indicator for bed stability, over a range of $\Delta x = 150 - 450$ μm. Smoothing is conducted by solving the diffusion-type equation given in Eq. (7). The local smoothing length L_s is set based on the local maximum particle diameter (Eq. (8)), as recommended by Sun and Xiao (2015a,b). In cells without particles, the minimum particle diameter was used. The scaling parameter λ determines the smoothing strength. A very similar approach was recently demonstrated by Huang et al. (2023). Based on their and others (Esteghamatian et al., 2018; Sun and Xiao, 2015b) results, we set the smoothing length to $\lambda = 3$, which is commonly reported as optimal.

$$\frac{d\bullet}{dt} = \frac{L_s^2}{\Delta t_{\text{CFD}}} \nabla^2 \bullet \tag{7}$$

$$L_s(x,t) = \begin{cases} \lambda \cdot d_{p,\max}(x,t) & \varepsilon_f(x,t) < 1 \\ \lambda \cdot d_{p,\min} & \varepsilon_f(x,t) = 1 \end{cases} \tag{8}$$

Lastly, the $\partial\epsilon/\partial t$ term in the continuity equation (Eq. (1)) is known to cause instability in the flow solution (Peng et al., 2014). This effect is especially strong as we apply a cell size smaller than the largest particles, and employ spatial, but no temporal smoothing. A common solution is to omit this term from the continuity equation (El Geitani et al., 2023). In a physical sense, this can be viewed as assuming the fluid motion is much faster than the particle movement, such that the particle configuration can be presumed steady-state during the flow solution. As we show in our results, this is a valid assumption for the current system. Therefore, we have omitted the first term in Eq. (1).

2.3. Simulation set-up

All simulations presented in this work were performed using the open-source CFD-DEM framework CFDEMCoupling (Goniva et al., 2012), based on LIGGGHTS (Kloss et al., 2012) and OpenFOAM (Weller et al., 1998). A 10 mm diameter column geometry was used as a base case, corresponding to the smaller columns used in previous experimental work (e.g. Ghose et al., 2000) and encompassing roughly 1 million individual particles. Calculations were performed on the Dutch national supercomputer Snellius, using 64 CPUs in a $2 \times 2 \times 16$ grid arrangement and 112 GB of memory. This enabled a computational speed of 0.55 s of simulation time per hour of computational time.

Table 1 provides a detailed overview of all material properties and settings used in the base case simulation. Material properties are based on values commonly found in literature, as indicated by the references in the table. Fig. 1 shows a schematic overview of the simulation geometry, for cylindrical ($\alpha = 0$ deg) and tapered ($\alpha > 0$ deg) cases. In the tapered case, the base diameter D_0 and settled bed volume $V_{b,0}$ were set equal to the cylindrical base case. The inlet velocity was increased such that the expanded bed volume V_b was equal as well, thereby maintaining equal volumetric expansion $V_b/V_{b,0}$.

Table 2 lists all simulations performed. Each case represents a singular adjustment with respect to the base case #1, i.e. all other settings remained constant. This ensures the influence of each adjusted parameter can be assessed independently. With increasing case number, the simulations are used to assess the influence of the expansion factor, liquid viscosity, bed aspect ratio (adjusting both H_0 and D to maintain a constant bed volume), particle density, particle density distribution width, particle size distribution width, column taper angle and column alignment angle, respectively. The inlet velocity U_0 in each case was set based on a prediction of the desired expansion H/H_0^{pred} by the Richardson-Zaki equation (Richardson and Zaki, 1997), as explained in Section 2.3.1. For comparison, we have also included the actual obtained expansion H/H_0.

2.3.1. Initialisation

To aid computational efficiency, the simulations were initialised in expanded state, such that the initial expansion from packed state

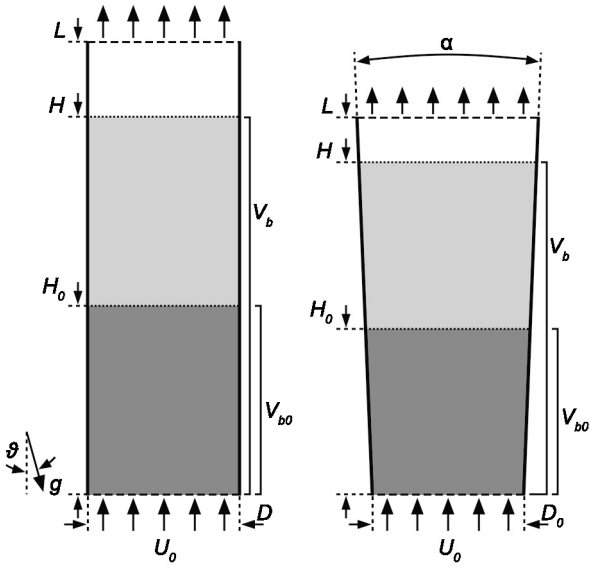

Fig. 1. Schematic overview of cylindrical (left) and tapered (right) columns, showing the bed settled (dark grey) and expanded (light grey) states.

Table 2
List of simulation cases. Each represents a singular adjustment with respect to the base case #1. Superficial inlet velocities are estimated through the Richardson-Zaki equation (Eq. (9) Richardson and Zaki, 1997).

ID	Description	U_0 (mm/s)	H/H_0 (-)
#01	Base case	1.42	1.82
#02	$H/H_0^{\text{pred}} = 1.5$	0.80	1.09
#03	$H/H_0^{\text{pred}} = 3.0$	2.22	2.80
#04	$H/H_0^{\text{pred}} = 4.0$	2.57	3.80
#05	$H/H_0^{\text{pred}} = 5.0$	2.69	4.68
#06	$\nu_f = 2.0 \cdot 10^{-6}$ m^2/s	0.71	1.81
#07	$\nu_f = 4.0 \cdot 10^{-6}$ m^2/s	0.36	1.81
#08	$H_0/D = 2.5$	1.42	1.82
#09	$H_0/D = 7.5$	1.42	1.82
#10	$H_0/D = 10.0$	1.42	1.81
#11	$\langle\rho_p\rangle = 1250$ kg/m^3	0.71	1.81
#12	$\langle\rho_p\rangle = 2000$ kg/m^3	2.83	1.84
#13	$\langle\rho_p\rangle = 3000$ kg/m^3	5.58	1.83
#14	$\sigma_{\rho p} = 125$ kg/m^3	1.42	1.95
#15	$\sigma_{\rho p} = 250$ kg/m^3	1.42	2.12
#16	$w = 1/2$	1.33	1.79
#17	$w = 1/8$	1.57	1.82
#18	$\alpha = 2.5$ deg	2.06	1.19
#19	$\vartheta = 0.5$ deg	1.42	1.59
#20	$\vartheta = 1.0$ deg	1.42	1.38

need not be simulated. The continuous lognormal particle size distribution was discretised into fractions of equal area, as shown in Fig. 2. The local voidage of each fraction in expanded state was estimated through the Richardson-Zaki equation (Eq. (9)-(10)) (Richardson and Zaki, 1997; Kramer et al., 2019), where $|\vec{u}_0|$ is the superficial velocity and $|\vec{u}_t|$ the terminal velocity. The latter was obtained from the force balance in Eq. (11). Here, $\text{Re}_t = \rho_f |\vec{u}_t| d_p / \eta_f$ is the terminal Reynolds number, $\text{Ar} = d_p^3 \rho_f (\rho_p - \rho_f) |\vec{g}| / \eta_f^2$ the Archimedes number, and C_D the drag coefficient calculated through the Schiller-Naumann drag model (Eq. (12) (Shiller and Naumann, 1935)). The fractions are then stacked upon each other to obtain a perfectly stratified initial bed state. This method was previously shown by Yun et al. (2004c) to provide an accurate estimation of the total bed expansion. Iterating this approach allowed to determine the superficial inlet velocity U_0 required for the

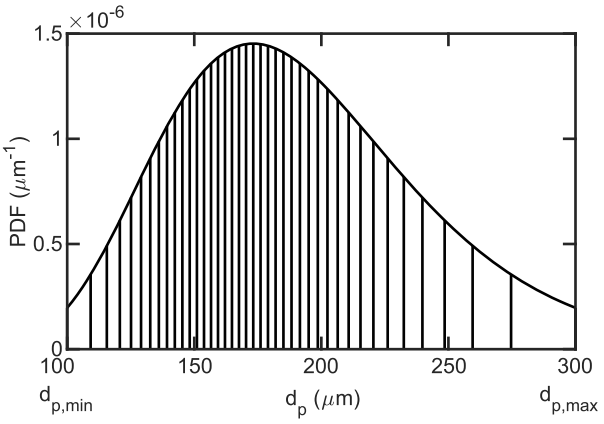

Fig. 2. Lognormal particle size distribution.

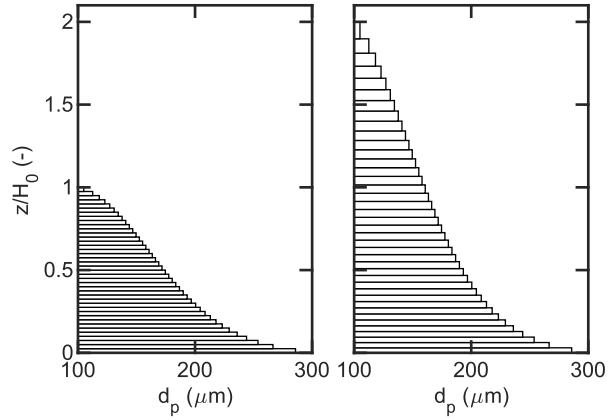

Fig. 3. Initial stratified bed structure in packed (left) and expanded (right) states, as estimated from the Richardson-Zaki equation (Eq. (9) (Richardson and Zaki, 1997)).

desired expansion. Fig. 3 shows the resulting bed structure in packed and expanded states, at an predicted expansion factor of $H/H_0^{\text{pred}} = 2.0$.

$$\varepsilon^n = \frac{|\vec{u}_0|}{|\vec{u}_t|} \tag{9}$$

$$n = \begin{cases} 4.65 & \text{for} \quad \text{Re}_t < 0.2 \\ 4.4 \cdot \text{Re}_t^{-0.03} & \text{for} \quad 0.2 \leq \text{Re}_t < 1.0 \\ 4.4 \cdot \text{Re}_t^{-0.1} & \text{for} \quad 1.0 \leq \text{Re}_t < 500 \\ 2.4 & \text{for} \quad \text{Re}_t \geq 500 \end{cases} \tag{10}$$

$$\frac{3}{4}\text{Re}_t^2 \cdot C_D\left(\text{Re}_t\right) = \text{Ar} \tag{11}$$

$$C_D\left(\text{Re}\right) = \max\left[\frac{24}{\text{Re}}\left(1 + 0.15 \cdot \text{Re}^{0.687}\right), 0.44\right] \tag{12}$$

3. Results and discussion

In this section, we will first describe the liquid flow and particle behaviour in the base case #1. Next, we will highlight the most important changes to that behaviour resulting from property adjustments listed in Table 2. Additional information is provided in Table A.1.

Fig. 4 shows the structure of the expanded bed by its axial voidage and particle size distributions. As expected, there is a voidage gradient over the height of the bed, ranging from almost packed close to the inlet, to a dilute region near the top of the bed. The temporal standard deviation, indicated by the dashed lines, shows that this structure is very stable over time. The mean particle size follows the curve shape

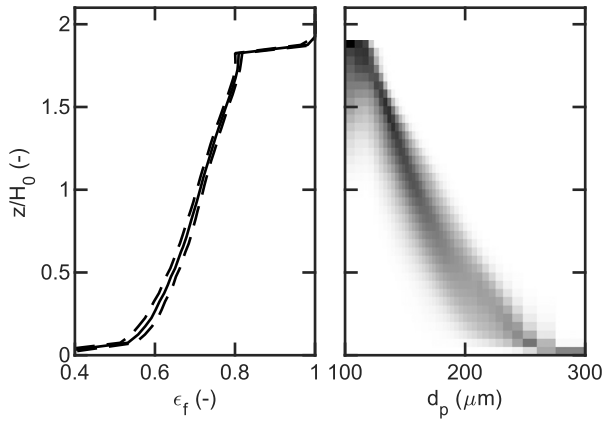

Fig. 4. Left: time-averaged axial voidage profile (case 1). Dashed lines indicate temporal standard deviation. Right: time-averaged axial particle size distribution (case #1).

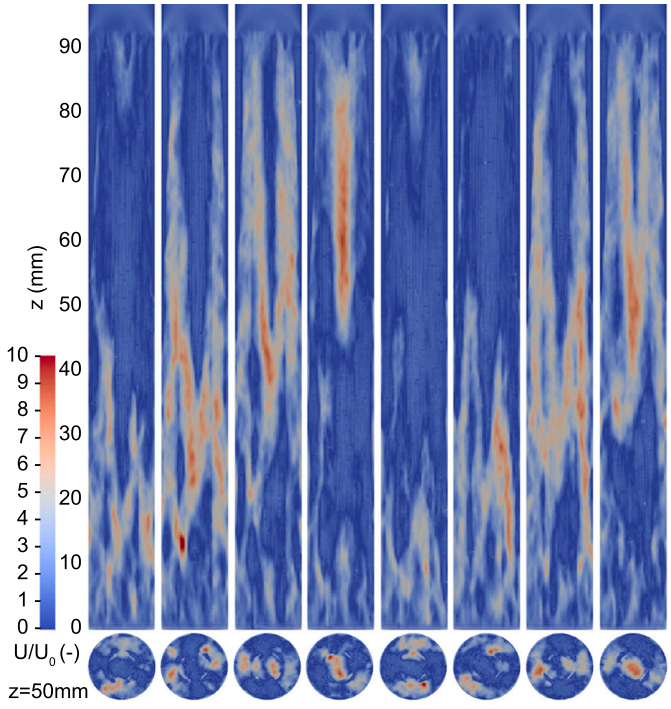

Fig. 5. Vertical (top) and horizontal (bottom) cross-sections of instantaneous liquid flow profile (case #1). Snapshots are taken 0.4 s apart.

predicted in Fig. 3. It is clear that there is some degree of mixing, resulting in a local particle size distribution, rather than a perfectly classified bed. Tong and Sun (2002b) measured the local particle size distribution experimentally, and found a local distribution width between 35% and 50% of the global distribution, widening towards to bottom of the bed. These findings correspond very well with our current observations.

It has been noted before that flow heterogeneities can play a significant role even in liquid-solid fluidisation (Nijssen et al., 2021). The liquid flow snapshots in Fig. 5 show plume-like heterogeneities, which stretch over the length of the bed and move in spiralling motion, reminiscent of the bubble plumes found in slurry bubble columns (Warsito and Fan, 2005). To the best of our knowledge, this behaviour has not been previously reported for liquid-solid fluidised beds.

The liquid velocity in these plumes reaches up to 10× the superficial velocity, while the movement of the plumes themselves is much faster than the liquid in them. This suggests that the compressibility of the suspension plays a large role in their propagation. It is not within the scope

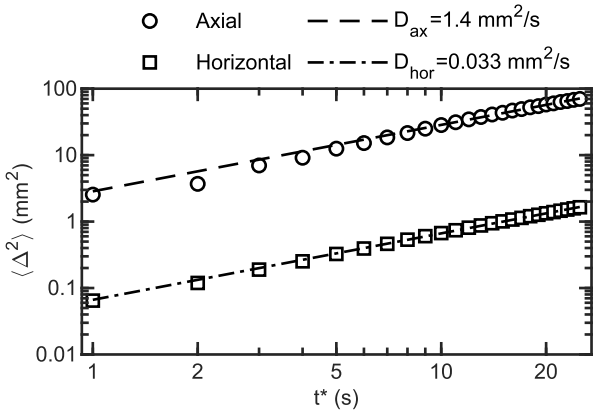

Fig. 6. Axial and horizontal mean particle displacement (case #1). Dashed lines indicate fitted dispersion coefficients.

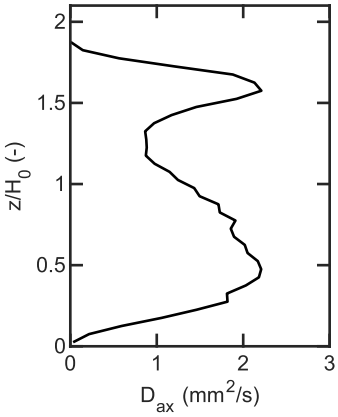

Fig. 7. Local axial solids dispersion coefficient over bed height (case #1).

of the current work to investigate the origin of these flow structures, but these findings definitely warrant a more fundamental investigation into the interaction between the solid and liquid phases.

The movement of particles is a strong indicator of the stability of the expanded bed. For optimal performance in a chromatography process, it is desirable to prevent any large-scale motion of particles. This is quantified by the solids dispersion coefficient D, which is obtained from the mean squared particle displacement $\langle\Delta^2\rangle$ over an interval t^* per Eq. (13) (Parker et al., 1997).

$$\langle\Delta^2\rangle = 2Dt^* \tag{13}$$

Fig. 6 shows the particle displacement and the dispersion coefficients obtained from it. It is clear that the mean squared displacement follows a linear trend, which indicates the presence of random Brownian-like motion and the absence of net, large-scale particle movement. The horizontal and axial dispersion have been measured separately. There exists a large separation of scales between these motions; the dispersion in the axial direction is two orders of magnitudes stronger than in the horizontal direction. Ewert (2016) experimentally measured solids dispersion coefficients in expanded bed columns using PEPT. While direct comparison the dispersion coefficient is precarious, as particle sizes and densities differ, the value obtained here ($D = 1.4$ mm^2/s) corresponds very well with the range of values found by Ewert (0.5 - 6 mm^2/s).

As the CFD-DEM technique provides information on all particles within the bed simultaneously (as opposed to a single tracer particle in experimental tracking methods like PEPT), it is possible to accurately measure the local dispersion coefficient in a certain portion of the bed. Fig. 7 shows the axial solids dispersion coefficient over the height of the

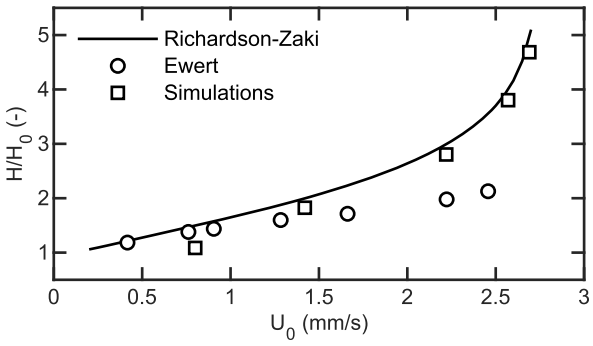

Fig. 8. Expansion curve, including Richardson-Zaki prediction (Richardson and Zaki, 1997), experimental results by Ewert (2016), and the current simulations (cases #1-5).

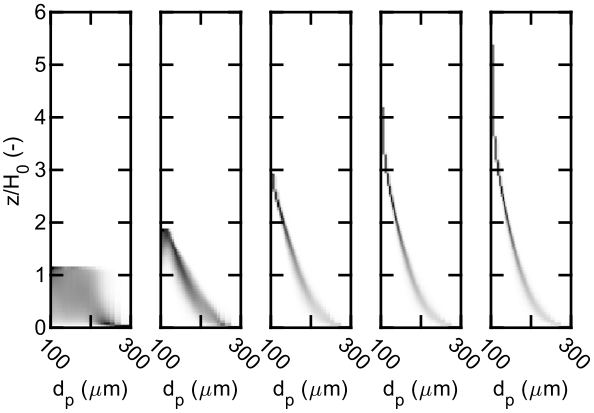

Fig. 9. Time-averaged axial particle size distribution at increasing expansion. From left to right: case #2, 1, 3, 4, and 5.

bed. Two distinct maxima exist, around 20% and 90% of the expanded bed height, with a minimum around 70% of the bed height. This corresponds very well with measurements of liquid mixing by Lin et al. (2015), who reported a low-mixing zone between 60-80% of the expanded bed height. Contrarily, Ewert (2016) reported the inverse shape, with a maximum at around 60% of the expanded bed height. However, as noted before, this was based on the movement of a single tracer particle, which resulted in significant scatter of data and lack of clear trends.

3.1. Influence of expansion factor

The expansion factor is one of the most important operational parameters for an expanded bed process. In Fig. 8, the expansion curve based on cases #1-5 is shown, alongside the prediction by Richardson and Zaki (1997) as elaborated in Section 2.3.1, and experimental results for similar size and density particles reported by Ewert (2016). For this measurement, the expanded bed height was defined as the height under which 99% of the bed mass was contained. The numerical results correspond very well with the Richardson-Zaki model, with expansions being slightly lower than predicted. As shown by Ren et al. (2021), the obtained expansion is sensitive to the exact drag model used. Furthermore, the simulations exhibit a finite degree of mixing, as opposed to the perfect stratification assumed in the prediction. The largest deviation is found at the lowest expansion where, as shown in Fig. 9, mixing is strongest. At higher expansions, there is a strong deviation between the experimental results by Ewert (2016) and both simulations and the Richardson-Zaki model. This was also remarked by Ewert, who suggested that the column might not be perfectly aligned in these experiments. As shown in Section 3.7, column misalignment can cause major collapse of the bed, explaining the deviation. We therefore conclude that our model exhibits accurate expansion behaviour.

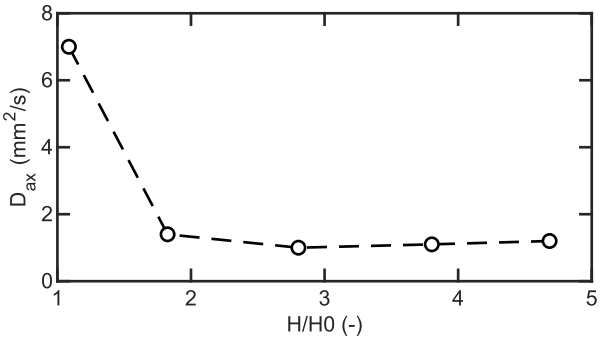

Fig. 10. Axial solids dispersion coefficient versus expansion factor (cases #1-5).

Fig. 9 shows the axial particle size distribution for an increasing expansion factor. At the lowest expansion we observed strong mixing and a loss of expansion. In this dense case, the mean-free-path between particle collisions is short, leading to frequent, low-velocity collisions (Aguilar-Corona et al., 2011) and rapid dissipation of kinetic energy by lubrication forces (Liu et al., 2016). Clearly, these effects are stronger than the fluid-particle interaction separating the particles at this lowest liquid velocity. At higher liquid velocities, particle mixing is strongly reduced, leading to sharper particle size distributions. However, beyond an expansion factor of $H/H_0 = 3$, no significant improvement in bed stability is observed. This is also reflected by the solids dispersion coefficients shown in Fig. 10. It was previously observed experimentally (Al-Dibouni and Garside, 1979; Kaluderović Radoicić et al., 2014) and numerically (Liu et al., 2016; Nijssen et al., 2021), and confirmed by these results that solids mixing does not increase monotonically with liquid velocity, as is often assumed (e.g. van der Meer et al., 1984).

Our results suggest that operating at higher expansions is undesirable, as the highly dilute bed makes inefficient use of the column volume, at no gain of bed stability. Based this, the optimal operation is between expansion factors of 2-3, coinciding with the recommendation of Xia et al. (2007). It should be noted that the solids dispersion coefficients provide no conclusive results on liquid dispersion. While the two are obviously related, there is an additional degree of sub-grid liquid mixing associated with the flow through the array of particles, which is presently not accounted for. This mixing mechanism grows stronger with increasing liquid velocity (e.g. Buyuktas and Wallender, 2004), leading to reduced separation performance at higher expansion. This further confirms the recommendation to operate at intermediate expansions.

3.2. Influence of viscosity

Figs. 11 and 12 show instantaneous flow cross-sections for the two cases with increased viscosity (cases #6 and 7), similar to the base case #1 shown in Fig. 5. With higher viscosity, the plume-like, spiralling flow heterogeneities grow stronger and more stable. In cases #6 and 7, four separate plumes can be distinguished, which rotate and alternately split and merge. The increased stability of these structures can be explained by the stronger dampening of particle-particle interactions (Nijssen et al., 2023b), which results in less random particle motion to disturb the flow pattern. Additionally, the period of the spiralling motion increases with viscosity.

A larger fraction of the liquid travels through the plumes at increased viscosity, as indicated by the higher maximum normalised velocity U/U_0. This might negatively impact chromatography performance, as it widens the liquid residence time distribution. Such undesired behaviour at high viscosity was also experimentally observed by Chase and Draeger (1992a). Interestingly, despite the stronger flow heterogeneity, solids mixing weakens with increasing viscosity. The solids dispersion coefficients are shown in Fig. 13 alongside the solids Bodenstein number $\mathrm{Bo} = U_0 H / D_{\mathrm{ax}}$, indicating the balance between liquid

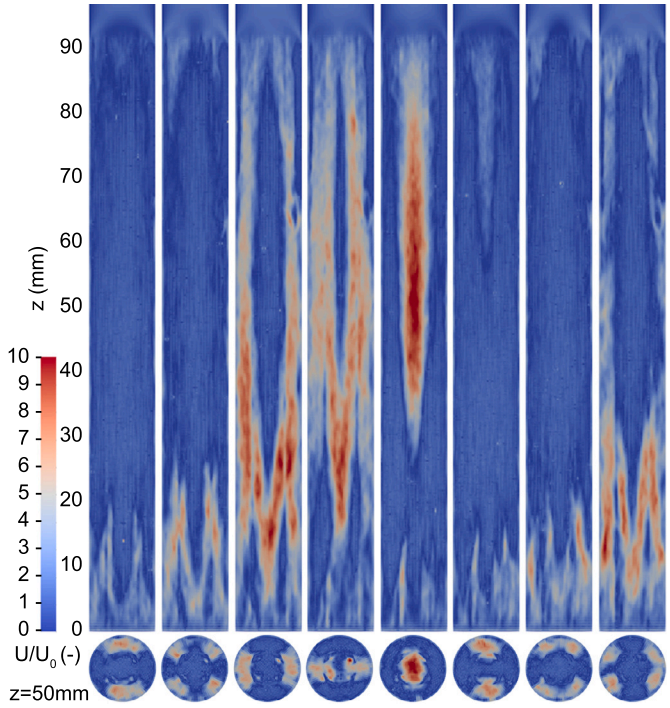

Fig. 11. Vertical (top) and horizontal (bottom) cross-sections of instantaneous liquid flow profile (case #6). Snapshots are taken 0.4 s apart.

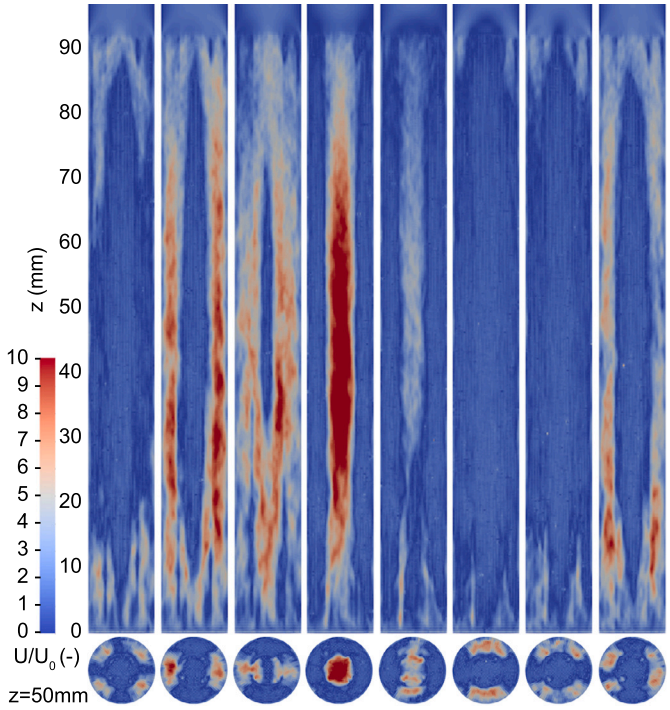

Fig. 12. Vertical (top) and horizontal (bottom) cross-sections of instantaneous liquid flow profile (case #7). Snapshots are taken 0.4 s apart.

convection and solids dispersion. A decreasing dispersion coefficient might be expected from the decreasing liquid viscosity, but the strongly increasing Bodenstein number indicates that solids mixing decreases much quicker than the liquid flow velocity. This might be attributed to the strong dampening of particle-particle interactions due to the interstitial liquid (Nijssen et al., 2023b). However, the influence these lubrication forces on the global bed behaviour and particle mixing is

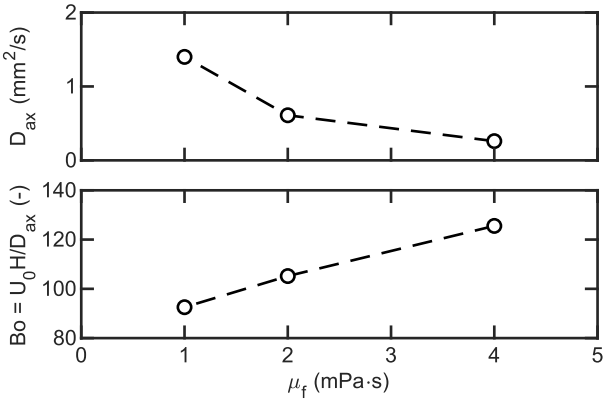

Fig. 13. Axial solids dispersion coefficient (top) and solids Bodenstein number (bottom) over liquid viscosity, at constant expansion factor (cases #1, 6, and 7).

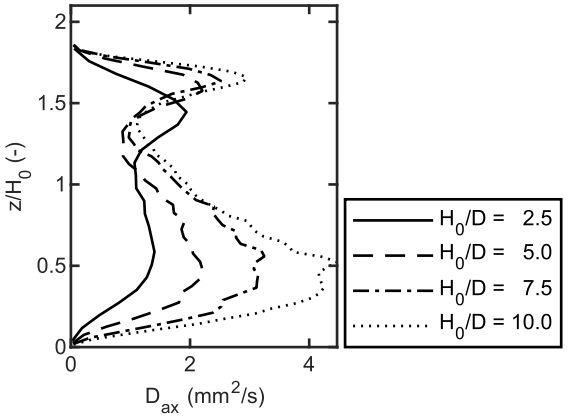

Fig. 14. Local axial solids dispersion coefficient over bed height for various bed aspect ratios (cases #1, 8, 9, and 10).

not yet completely clear (Liu et al., 2016). Further in-depth research is required to provide a definitive answer to this open question.

3.3. Influence of aspect ratio

Cases #1, 8, 9, and 10 represent expanded beds with identical bed volume and expansion factor, but varying aspect ratio. Fig. 14 shows axial solids dispersion curves for all cases. These show an increase in particle dispersion with increasing aspect ratio, especially in the bottom half of the bed. Furthermore, there is a downward shift of the upper peak at the lowest aspect ratio. At a higher aspect ratio i.e. in a slimmer, longer column, the gradients describing stratification $d\varepsilon/dz$ and dd_p/dz are less steep, as they are stretched over a longer bed height. This means that particles have a larger mobility, since the driving force confining them to a specific height is weaker. This is clear from the mean axial dispersion coefficients, which are 1.0, 1.4, 2.0 and 2.5 mm^2/s for aspect ratios of 2.5, 5.0, 7.5 and 10.0, respectively.

Ghose and Chase (2000) observed a small decrease of liquid-phase mixing with increasing aspect ratio, though this was measured at constant packed bed height, rather than constant bed volume. Again, the link between solid-phase and liquid-phase mixing is non-trivial, and warrants further investigation. It should also be noted that flow distribution at the column entrance plays a significant role in liquid mixing (Jin, 2015). In simulations, uniform flow distribution is easily set. However, in practice this is more precarious, especially in larger diameter columns (Jin, 2015).

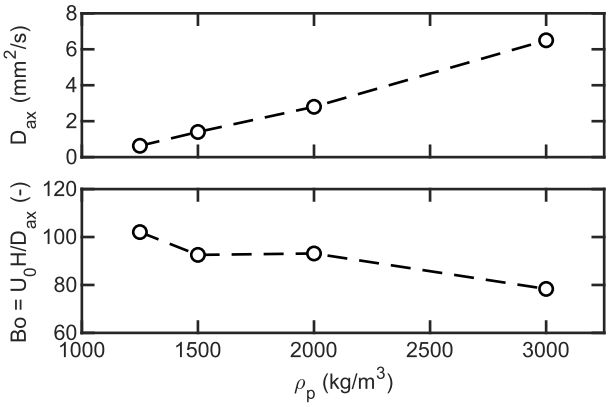

Fig. 15. Axial solids dispersion coefficient (top) and solids Bodenstein number (bottom) over particle density, at constant expansion factor (cases #1, 11, 12, and 13).

3.4. Influence of particle density

In this work, we have varied both the uniform particle density, as well as the width of a non-uniform particle density distribution. In the former case the expanded bed volume was kept constant by increasing the liquid velocity along with the particle density (see Table 2). The solids mixing behaviour in these simulations is summarised in Fig. 15. It is clear that the solids dispersion coefficient strongly increases with particle density, as both the increased particle inertia and increased liquid velocity lead to stronger particle motion. However, the increased density also allows for a higher liquid throughput. Remarkably, the solids dispersion increases 8-fold over the simulated density range, while the Bodenstein numbers remain within a 25% range. Between $\rho_p = 1,500$ kg/m^3 (case #1) and $\rho_p = 2,000$ kg/m^3 (case #12), we even obtained identical Bodenstein numbers (Bo = 93), despite the throughput being twice as high in the latter case. This shows that developing higher-density particles is vital for achieving improved throughput (Pålsson et al., 2000), and that EBA can be operated at higher flowrate without prohibitive loss of bed stability.

In cases #14 and 15, Gaussian density distributions were applied, while maintaining identical bed mass and flow rate to case #1. This led to wash-out of some of the small, low-density particles with terminal velocities below the superficial velocity. Afterwards, a stable bed was obtained, of which the voidage, particle size, and particle density distributions are shown in Fig. 16. In these cases, the bed is stratified by both size and density, leading to a wider local distributions for both. However, as can be seen from the increasingly smooth voidage distribution, the effects of size and density combine to form a more stable bed than for a uniform density. This is clearly reflected by the dispersion coefficients, which were found 1.4, 0.83, and 0.49 mm/s^2 for the uniform distribution (case #1), $\sigma_{\rho p} = 125$ kg/m^3 (case #14), and $\sigma_{\rho p} = 250$ kg/m^3 (case #15), respectively. This confirms experimental results by Tong and Sun (2002b) and Pålsson et al. (2000), who both observed decreased liquid mixing for wider density distributions.

3.5. Influence of particle size distribution

The width of the particle size distribution is an important parameter, as it sets the driving force for bed stratification. In cases #16 and 17, a narrower and a wider size distribution were tested. It should be noted that the mean, minimum, and maximum particle sizes were kept constant, which can be interpreted as using the same sieve fraction. This was done as inserting much larger or smaller particles into the simulation negatively impacts numerical stability. The resulting axial particle size distributions are shown in Fig. 17. It is clear that the wide size distribution (case #16) does not provide a significant improvement in bed stability. However, the narrow size distribution (case #17) results

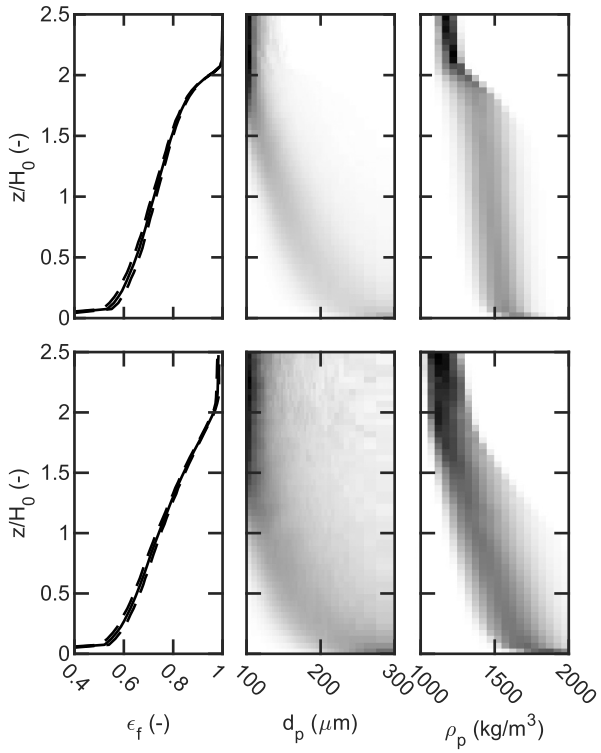

Fig. 16. Left: time-averaged axial voidage profile. Dashed lines indicate temporal standard deviation. Middle: time-averaged axial particle size distribution (case #1). Right: time-averaged axial particle density distribution. Top: $\sigma_{\rho p} = 125$ kg/m^3 (case #14). Bottom: $\sigma_{\rho p} = 250$ kg/m^3 (case #15).

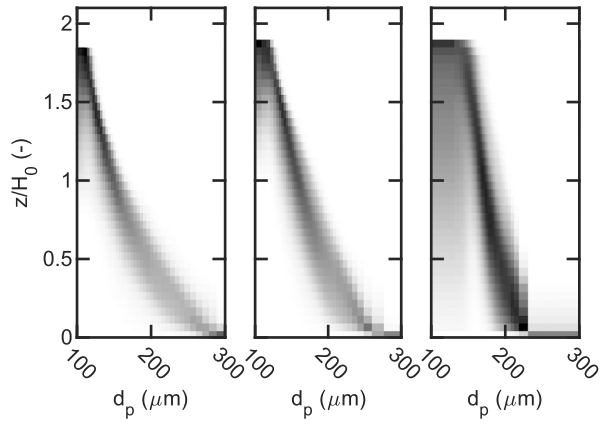

Fig. 17. Time-averaged axial particle size distribution at decreasing distribution width. From left to right: case #16, 1, and 17.

in enhanced mixing, especially of the smaller particles. The resulting solids dispersion coefficients were 1.4, 1.4, and 3.8 mm^2/s for $w = 1/2$, 1/4, and 1/8, respectively. This shows the importance of a wide enough particle size distribution to obtain a stable classified bed.

3.6. Influence of taper angle

Tapered liquid-solid fluidised beds are often employed as bioreactors (e.g. Koerich et al., 2020). The increasing cross-sectional area and therefore decreasing liquid velocity allows for higher throughputs without risking loss of small particles. In case #18, a 2.5 degree taper angle was applied. Fig. 18 shows a cross-section of the time-averaged solids mass flux and voidage profiles. It is obvious that the tapered geometry leads to strong solids circulation, and formation of dense, downward moving

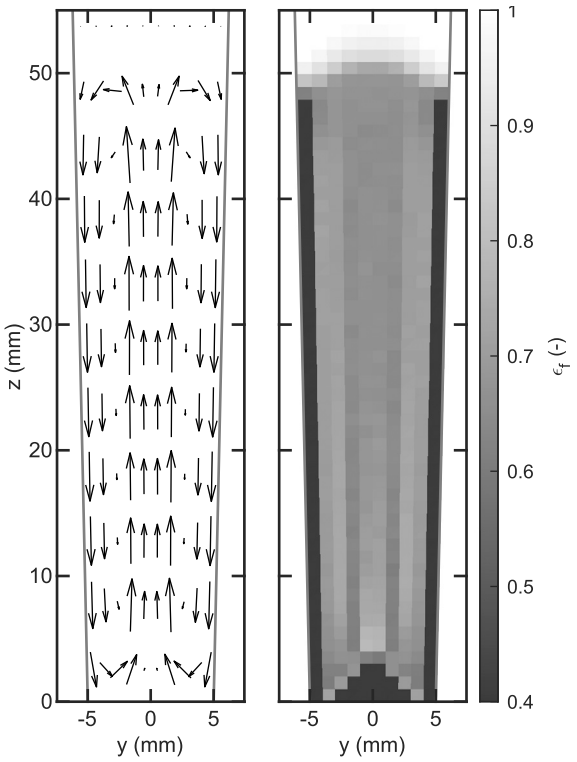

Fig. 18. Time-averaged solids flux profile (left) and time-averaged voidage profile (right) for tapered column (case #18).

zones close to the walls. This results in bed collapse, large-scale mixing, and liquid bypassing the particles close to the wall. Quickly after the start of the simulation, a completely mixed state of the bed is achieved, which then remains stable in time. It is therefore not recommended to further pursue tapered geometries for application in Expanded Bed Adsorption.

3.7. Influence of column alignment

The importance of proper column alignment is well-known for liquid-solid fluidisation. For example, Bruce et al. (1999) observed the liquid Bodenstein number in an EBA column to drop from 140 to 50 for a misalignment as little as 0.15 deg. Ewert (2016) also showed the emergence of large-scale circulation patterns in misaligned columns. In cases #19 and 20, we have simulated columns misaligned by 0.5 and 1 deg, respectively. Fig. 19 shows time-averaged solids mass flux and voidage cross-sections for these cases. In both cases, a particle-dense zone appears at the wall on the low side of the column. This gives rise to a circulation pattern where particles move up through the column, then down through this dense zone. At 0.5 deg misalignment this pattern is still mostly concentrated at the low side of the column. At $\vartheta = 1.0$ deg, the circulation encompasses the whole column. Column misalignment leads to strong mixing of particle and collapse of the bed, as seen from the bed heights and solids dispersion coefficients listed in Table 3. At 1 degree of misalignment the expanded bed height drops by 25%, while particle dispersion grows 14× stronger. These results highlight the vital importance of proper column alignment, even for columns as small as 1 cm diameter simulated here.

4. Conclusions

In this work, we have used CFD-DEM to study the hydrodynamics of the Expanded Bed Adsorption process. We showed that particle mixing decreases with increasing bed expansion, though with diminishing improvements in very dilute columns, leading to an optimal operation

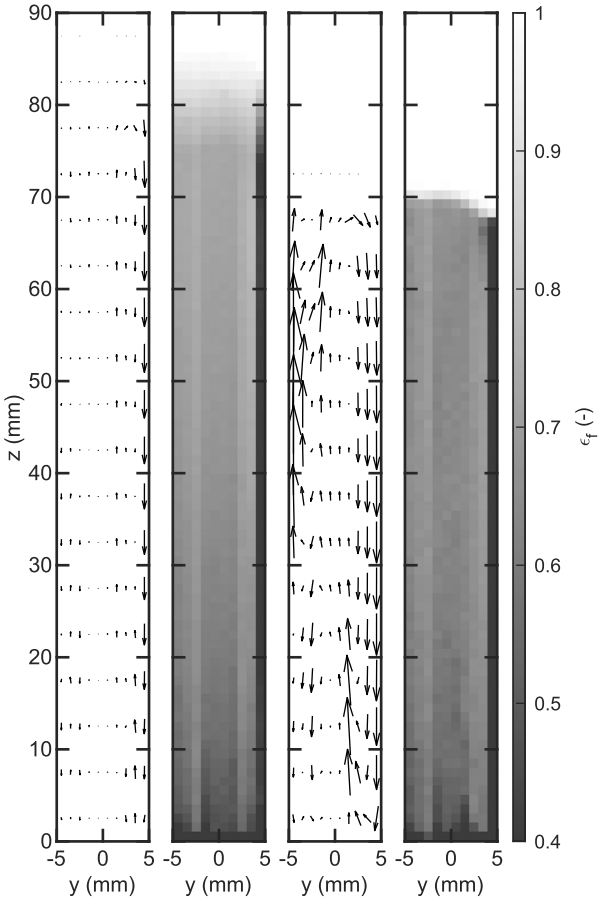

Fig. 19. Time-averaged solids flux profile and time-averaged voidage profile for misaligned column. Left: $\alpha = 0.5$ deg (case #19). Right: $\alpha = 1.0$ deg (case #20).

Table 3
Bed height and solids dispersion coefficient for various column alignment angles (cases #1, 19, and 20).

ϑ (deg)	H (mm)	D_{ax} (mm^2/s)
0.0	91	1.4
0.5	80	5.0
1.0	69	19.9

window between 2-3× expansion. Highly viscous feedstocks gave rise to stable swirling flow patterns, which might negatively impact column performance. Simultaneously, solids dispersion was found to decrease, highlighting the complex relationship between liquid and solids mixing. Increased particle density resulted higher liquid throughput, but also stronger mixing. Yet, stable expanded beds were achieved with particle densities as high as 3,000 kg/m^3. Furthermore, the superposition of a particle size distribution and particle density distribution greatly improved bed stability. Overall, it was found that mixing in the expanded column, of both the liquid and solid phases, is a complex process, which cannot be simply predicted from the flow velocity.

The simulations were also used to test various column designs. The aspect ratio of the bed was found to influence particle motion in the lower half of the bed. Use of a tapered column leads to very strong circulation patterns, and is therefore not recommended. Lastly, the importance of proper column alignment was shown, as misalignment leads to circulation, mixing, and loss of expansion. With this study, we have demonstrated the usefulness of physics-based numerical methods such as CFD-DEM for process development.

5. Outlook

The results in this work have yielded many directions for future research. The swirling fluid motion observed at high viscosity warrants a more fundamental investigation into the origin and stability of these structures. On a more practical side, the transient behaviour of the bed at initial expansion, sedimentation, as well as during liquid phase switching between processing steps is an interesting area for further study. Lastly, the role of particle-particle cohesion caused by the presence of cell material is another area where CFD-DEM can provide valuable information for process design.

In order to truly assess the chromatographic capacity of the column, additional calculations need to be integrated into the model. Firstly, sub-grid liquid dispersion is expected to be of great importance. An appropriate model for this effect would need to consider the local distribution of particles (Buyuktas and Wallender, 2004), relative velocity between particles and fluid, as well as the motion of particles with respect to each other (granular temperature Goldhirsch, 2008). Next, the adsorption equilibria and mass transfer rates need to be included into the model (Wright and Glasser, 2001). A final challenge is posed by the separation of time scales between the hydrodynamics effects and the adsorption process. Fully simulating both simultaneously would lead to prohibitively long computational times. We therefore recommend to separate these time scales, for example using the recurrence CFD (rCFD) method (Lichtenegger and Pirker, 2016).

Declaration of competing interest

The authors declare that they have no known competing financial interests or personal relationships that could have appeared to influence the work reported in this paper.

Data availability

The raw simulation output from this work is openly available at 4TU.ResearchData (Nijssen et al., 2023a).

Acknowledgement

We are grateful to S. Pirker, D. Queteschiner, T. Lichtenegger and the Particulate Flow Modelling group at JKU Linz for their continual collaboration in the CFDEMCoupling framework.

Funding acknowledgement

This work was supported by the Dutch Research Council NWO [grant number 729.001.002], and made use of the Dutch national e-infrastructure with the support of the SURF Cooperative [grant number EINF-3414].

Appendix A

Table A.1
Superficial liquid velocity, total bed mass, bed height, axial and horizontal solids dispersion coefficients for all cases.

ID -	U_0 mm/s	M_p g	H mm	D_{ax} mm^2/s	D_{hor} mm^2/s
#01	1.42	3.37	91.2	1.4	0.033
#02	0.80	3.37	54.3	7.1	0.049
#03	2.22	3.37	140.2	1.0	0.042
#04	2.57	3.36	190.1	1.1	0.049
#05	2.69	3.37	234.2	1.2	0.047
#06	0.71	3.37	90.4	0.61	0.014
#07	0.36	3.37	90.7	0.26	0.0058
#08	1.42	3.38	57.5	1.0	0.045
#09	1.42	3.34	118.9	2.0	0.036
#10	1.42	3.34	143.2	2.5	0.037
#11	0.71	2.81	90.6	0.63	0.015
#12	2.83	4.49	92.1	2.8	0.076
#13	5.58	6.74	91.3	6.5	0.22
#14	1.42	3.37	97.3	0.82	0.023
#15	1.42	3.23	105.8	0.49	0.020
#16	1.33	3.37	89.5	1.4	0.037
#17	1.57	3.37	91.0	3.8	0.039
#18	2.06	3.37	49.9	12.7	0.49
#19	1.42	3.37	79.7	5.0	0.062
#20	1.42	3.37	68.9	19.9	0.28

References

Aguilar-Corona, A., Zenit, R., Masbernat, O., 2011. Collisions in a liquid fluidized bed. Int. J. Multiph. Flow 37 (7), 695–705. https://doi.org/10.1016/j.ijmultiphaseflow.2011.02.004.

Al-Dibouni, M.R., Garside, J., 1979. Particle mixing and classification in liquid fluidised beds. Trans. Inst. Chem. Eng. 57 (2), 94–103.

Bruce, L.J., Chase, H.A., 2002. The combined use of in-bed monitoring and an adsorption model to anticipate breakthrough during expanded bed adsorption. Chem. Eng. Sci. 57 (15), 3085–3093. https://doi.org/10.1016/S0009-2509(02)00179-3.

Bruce, L.J., Ghose, S., Chase, H.A., 1999. The effect of column verticality on separation efficiency in expanded bed adsorption. In: Expanded Bed Chromatography, pp. 69–75.

Buyuktas, D., Wallender, W.W., 2004. Dispersion in spatially periodic porous media. Heat Mass Transf. 40 (3–4), 261–270. https://doi.org/10.1007/s00231-003-0441-0.

Chang, Y.K., Chase, H.A., 1996. Development of operating conditions for protein purification using expanded bed techniques: the effect of the degree of bed expansion on adsorption performance. Biotechnol. Bioeng. 49 (5), 512–526. https://doi.org/10.1002/(SICI)1097-0290(19960305)49:5<512::AID-BIT4>3.3.CO;2-X.

Chase, H.A., Draeger, N.M., 1992a. Affinity purification of proteins using expanded beds. J. Chromatogr. A 597 (1–2), 129–145. https://doi.org/10.1016/0021-9673(92)80103-2.

Chase, H.A., Draeger, N.M., 1992b. Expanded-bed adsorption of proteins using ion-exchangers. Sep. Sci. Technol. 27 (14), 2021–2039. https://doi.org/10.1080/01496399208019462.

Crowe, C.T., Schwarzkopf, J.D., Sommerfeld, M., Tsuji, Y., 2012. Multiphase Flows with Droplets and Particles. CRC Press, Boca Raton, FL.

de Araújo Padilha, C.E., de Araújo Padilha, C.A., de Santana Souza, D.F., de Oliveira, J.A., de Macedo, G.R., dos Santos, E.S., 2017. Recurrent neural network modeling applied to expanded bed adsorption chromatography of chitosanases produced by Paenibacillus ehimensis. Chem. Eng. Res. Des. 117, 24–33. https://doi.org/10.1016/j.cherd.2016.09.022.

Dennis, S.C., Singh, S.N., Ingham, D.B., 1980. The steady flow due to a rotating sphere at low and moderate Reynolds numbers. J. Fluid Mech. 101 (2), 257–279. https://doi.org/10.1017/S0022112080001656.

Di Felice, R., 1994. The voidage function for fluid-particle interaction systems. Int. J. Multiph. Flow 20 (I), 153–159. https://doi.org/10.1016/0301-9322(94)90011-6.

Di Renzo, A., Di Maio, F.P., 2004. Comparison of contact-force models for the simulation of collisions in DEM-based granular flow codes. Chem. Eng. Sci. 59 (3), 525–541. https://doi.org/10.1016/j.ces.2003.09.037.

Doeven, M., den Boer, P., 2011. EBA technology: enabling the direct capture of pharma proteins. Innov. Pharm. Technol. 36, 66–68.

Dorn, M., Schilde, C., Burmeister, C.F., Hekmat, D., 2017. Mechanical characterization of compressible chromatographic particles. Powder Technol. 320, 213–222. https://doi.org/10.1016/j.powtec.2017.07.043.

Draeger, N.M., Chase, H.A., 1990. Protein adsorption in liquid fluidized beds. Inst. Chem. Eng. Symp. Ser. 118, 161–172.

D'Souza, R.N., Azevedo, A.M., Aires-Barros, M.R., Krajnc, N.L., Kramberger, P., Carbajal, M.L., Grasselli, M., Meyer, R., Fernández-Lahore, M., 2013. Emerging technologies for the integration and intensification of downstream bioprocesses. Pharm. Bioprocess. 1 (5), 423–440. https://doi.org/10.4155/pbp.13.55.

D'Souza, R.N., Kakarla, P.B., Yelemane, V., Meyer, R., den Boer, P., Fernández-Lahore, M., 2017. Controlling cell adhesion in antibody purification by expanded bed adsorption chromatography. Sep. Purif. Technol. 183, 270–278. https://doi.org/10.1016/j.seppur.2017.03.002.

El Geitani, T., Golshan, S., Blais, B., 2023. Toward high-order CFD-DEM: development and validation. Ind. Eng. Chem. Res. 62 (2), 1141–1159. https://doi.org/10.1021/acs.iecr.2c03546.

Esteghamatian, A., Euzenat, F., Hammouti, A., Lance, M., Wachs, A., 2018. A stochastic formulation for the drag force based on multiscale numerical simulation of fluidized beds. Int. J. Multiph. Flow 99, 363–382. https://doi.org/10.1016/j.ijmultiphaseflow.2017.11.003.

Ewert, S., 2016. Development of robust expanded bed adsorption processes for cGMP manufacture of biopharmaceutical products. Ph.D. thesis. University of Birmingham.
Felderhof, B.U., 1991. Virtual mass and drag in two-phase flow. J. Fluid Mech. 225, 177–196. https://doi.org/10.1017/S002211209100201X.
Ghose, S., Chase, H.A., 2000. Expanded bed chromatography of proteins in small diameter columns. I. Scale down and validation. Bioseparation 9 (1), 21–28. https://doi.org/10.1023/A:1008193312969.
Ghose, S., Chase, H.A., Titchener-Hooker, N., 2000. Bed height monitoring and control for expanded bed chromatography. Bioprocess Eng. 23 (6), 701–708. https://doi.org/10.1007/s004499900192.
Goldhirsch, I., 2008. Introduction to granular temperature. Powder Technol. 182 (2), 130–136. https://doi.org/10.1016/j.powtec.2007.12.002.
Goniva, C., Kloss, C., Deen, N.G., Kuipers, J.A.M., Pirker, S., 2012. Influence of rolling friction on single spout fluidized bed simulation. Particuology 10 (5), 582–591. https://doi.org/10.1016/j.partic.2012.05.002.
Hjorth, R.A., 1997. Expanded-bed adsorption in industrial bioprocessing: recent developments. Trends Biotechnol. 15 (6), 230–235. https://doi.org/10.1016/S0167-7799(97)01045-7.
Huang, C.-C., van Oijen, J.A., Deen, N.G., Tang, Y., 2023. A particle-size dependent smoothing scheme for polydisperse Euler-Lagrange simulations. Chem. Eng. Sci. 277, 118765. https://doi.org/10.1016/j.ces.2023.118765.
Jahanshahi, M., Ghoreishi, A.A., Vasheghani-F, E., Khavarpour, M., Abedijaber, A., 2009. Comparative study of hydrodynamic behavior of liquid expanded bed adsorption: mathematical and short-cut methods. Braz. J. Chem. Eng. 26 (2), 299–306. https://doi.org/10.1590/S0104-66322009000200007.
Jin, Z., 2015. Expanded bed adsorption - challenges and advances in column and process design. Pharm. Eng. 35 (1), 1–12.
Kaluderović Radoicić, T., Duriš, M., Garić-Grulović, R., Arsenijević, Z., Grbavčić, Ž., 2014. Solid circulation rate and particle collisions in quasi two-dimensional water fluidized beds of spherical particles. Powder Technol. 253, 295–303. https://doi.org/10.1016/j.powtec.2013.11.038.
Keener, R.N., Fernandez, E.J., Maneval, J.E., Hart, R.A., 2008. Advancement in the modeling of pressure-flow for the guidance of development and scale-up of commercial-scale biopharmaceutical chromatography. J. Chromatogr. A 1190 (1–2), 127–140. https://doi.org/10.1016/j.chroma.2008.02.113.
Kloss, C., Goniva, C., Hager, A., Amberger, S., Pirker, S., 2012. Models, algorithms and validation for opensource DEM and CFD-DEM. Prog. Comput. Fluid Dyn. 12 (2/3), 140. https://doi.org/10.1504/PCFD.2012.047457.
Koerich, D.M., Lopes, G.C., Rosa, L.M., 2020. Numerical study on the hydrodynamics of a fluidized-bed of bioparticles in tapered bioreactors with square shape cross-section. Braz. J. Chem. Eng. 37 (1), 101–115. https://doi.org/10.1007/s43153-020-00010-4.
Koppejan, V.W., Ferreira, G.N., Lin, D.Q., Ottens, M., 2018. Mathematical modelling of expanded bed adsorption – a perspective on in silico process design. J. Chem. Technol. Biotechnol. 93 (7), 1815–1826. https://doi.org/10.1002/jctb.5595.
Kramer, O.J.I., de Moel, P.J., Baars, E.T., van Vugt, W.H., Padding, J.T., van der Hoek, J.P., 2019. Improvement of the Richardson-Zaki liquid-solid fluidisation model on the basis of hydraulics. Powder Technol. 343, 465–478. https://doi.org/10.1016/j.powtec.2018.11.018.
Lichtenegger, T., Pirker, S., 2016. Recurrence CFD – a novel approach to simulate multiphase flows with strongly separated time scales. Chem. Eng. Sci. 153, 394–410. https://doi.org/10.1016/j.ces.2016.07.036. arXiv:1606.00586.
Lihme, A., Hansen, M., Olander, M., Zafirakos, E., 2000. Expanded bed adsorption in the purification of biomolecules. In: Desai, M.A. (Ed.), Downstream Processing of Biomolecules: Methods and Protocols, pp. 121–139.
Lin, D.-Q., Kula, M.-R., Liten, A., Thömmes, J., 2003. Stability of expanded beds during the application of crude feedstock. Biotechnol. Bioeng. 81 (1), 21–26. https://doi.org/10.1002/bit.10298.
Lin, D.Q., Thömmes, J., Kula, M.R., Hubbuch, J.J., 2004. The influence of biomass on the hydrodynamic behavior and stability of expanded beds. Biotechnol. Bioeng. 87 (3), 337–346. https://doi.org/10.1002/bit.20118.
Lin, D.Q., Tong, H.F., van de Sandt, E.J., den Boer, P., Golubović, M., Yao, S.J., 2013. Evaluation and characterization of axial distribution in expanded bed. I. Bead size, bead density and local bed voidage. J. Chromatogr. A 1304, 78–84. https://doi.org/10.1016/j.chroma.2013.06.057.
Lin, D.Q., Shi, W., Tong, H.F., van de Sandt, E.J., den Boer, P., Ferreira, G.N., Yao, S.J., 2015. Evaluation and characterization of axial distribution in expanded bed: II. Liquid mixing and local effective axial dispersion. J. Chromatogr. A 1393, 65–72. https://doi.org/10.1016/j.chroma.2015.03.019.
Liu, G., Yu, F., Lu, H., Wang, S., Liao, P., Hao, Z., 2016. CFD-DEM simulation of liquid-solid fluidized bed with dynamic restitution coefficient. Powder Technol. 304, 186–197. https://doi.org/10.1016/j.powtec.2016.08.058.
Loth, E., 2008. Lift of a spherical particle subject to vorticity and/or spin. AIAA J. 46 (4), 801–809. https://doi.org/10.2514/1.29159.
Nijssen, T.M.J., Kuipers, J.A.M., van der Stel, J., Adema, A.T., Buist, K.A., 2020. Complete liquid-solid momentum coupling for unresolved CFD-DEM simulations. Int. J. Multiph. Flow 132, 103425. https://doi.org/10.1016/j.ijmultiphaseflow.2020.103425.
Nijssen, T.M.J., Kramer, O.J.I., de Moel, P.J., Rahman, J., Kroon, J.P., Berhanu, P., Boek, E.S., Buist, K.A., van der Hoek, J.P., Padding, J.T., Kuipers, J.A.M., 2021. Experimental and numerical insights into heterogeneous liquid-solid behaviour in drinking water softening reactors. Chem. Eng. Sci. X 11, 100100. https://doi.org/10.1016/j.cesx.2021.100100.
Nijssen, T.M.J., Padding, J.T., Ottens, M., 2023a. Data companion to: Hydrodynamics of Expanded Bed Adsorption studied through CFD-DEM. 4TU.ResearchData doi:10.4121/ebaf0dc5-d8d2-4eb7-8f28-21f7f9b2335c.
Nijssen, T.M.J., Ottens, M., Padding, J.T., 2023b. A note on the modelling of lubrication forces in unresolved simulations. Powder Technol. 413 (March 2022), 118017. https://doi.org/10.1016/j.powtec.2022.118017.
Pålsson, E., Gustavsson, P.E., Larsson, P.O., 2000. Pellicular expanded bed matrix suitable for high flow rates. J. Chromatogr. A 878 (1), 17–25. https://doi.org/10.1016/S0021-9673(00)00223-5.
Parker, D.J., Dijkstra, A.E., Martin, T.W., Seville, J.P., 1997. Positron emission particle tracking studies of spherical particle motion in rotating drums. Chem. Eng. Sci. 52 (13), 2011–2022. https://doi.org/10.1016/S0009-2509(97)00030-4.
Parmar, M., Annamalai, S., Balachandar, S., Prosperetti, A., 2018. Differential formulation of the viscous history force on a particle for efficient and accurate computation. J. Fluid Mech. 844 (1885), 970–993. https://doi.org/10.1017/jfm.2018.217.
Peng, Z., Doroodchi, E., Luo, C., Moghtaderi, B., 2014. Influence of void fraction calculation on fidelity of CFD-DEM simulation of gas-solid bubbling fluidized beds. AIChE J. 60 (6), 2000–2018. https://doi.org/10.1002/aic.14421.
Ren, P., Li, W., Yu, K., 2021. Computational fluid dynamics simulation of adsorption process in a liquid-solids fluidized bed. J. Environ. Chem. Eng. 9 (4), 105428. https://doi.org/10.1016/j.jece.2021.105428.
Richardson, J.F., Zaki, W., 1997. Sedimentation and fluidisation: Part I. Trans. Inst. Chem. Eng. 32, 35–53. https://doi.org/10.1016/S0263-8762(97)80006-8.
Shiller, L., Naumann, A., 1935. A drag coefficient correlation. Z. Ver. Dtsch. Ing. 77, 318–320.
Staby, A., Jacobsen, J.H., Hansen, R.G., Bruus, U.K., Jensen, I.H., 2006. Comparison of chromatographic ion-exchange resins. V. Strong and weak cation-exchange resins. J. Chromatogr. A 1118 (2), 168–179. https://doi.org/10.1016/j.chroma.2006.03.116.
Sun, R., Xiao, H., 2015a. Diffusion-based coarse graining in hybrid continuum-discrete solvers: theoretical formulation and a priori tests. Int. J. Multiph. Flow 77, 142–157. https://doi.org/10.1016/j.ijmultiphaseflow.2015.08.014. arXiv:1409.0001.
Sun, R., Xiao, H., 2015b. Diffusion-based coarse graining in hybrid continuum-discrete solvers: applications in CFD-DEM. Int. J. Multiph. Flow 72, 233–247. https://doi.org/10.1016/j.ijmultiphaseflow.2015.02.014. arXiv:1409.0022.
Tong, X.D., Sun, Y., 2002a. Nd-Fe-B alloy-densified agarose gel for expanded bed adsorption of proteins. J. Chromatogr. A 943 (1), 63–75. https://doi.org/10.1016/S0021-9673(01)01435-2.
Tong, X.D., Sun, Y., 2002b. Particle size and density distributions of two dense matrices in an expanded bed system. J. Chromatogr. A 977 (2), 173–183. https://doi.org/10.1016/S0021-9673(02)01390-0.
van der Meer, A.P., Blanchard, C.M., Wesselingh, J.A., 1984. Mixing of particle in liquid fluidised beds. Chem. Eng. Res. Des. 62 (4), 214–222.
Versteeg, H.K., Malalasekera, W., 1995. An Introduction to Computational Fluid Dynamics: The Finite Volume Method. Pearson, Harlow.
Volk, A., Ghia, U., Stoltz, C., 2017. Effect of grid type and refinement method on CFD-DEM solution trend with grid size. Powder Technol. 311, 137–146. https://doi.org/10.1016/j.powtec.2017.01.088.
Warsito, W., Fan, L.S., 2005. Dynamics of spiral bubble plume motion in the entrance region of bubble columns and three-phase fluidized beds using 3D ECT. Chem. Eng. Sci. 60 (22), 6073–6084. https://doi.org/10.1016/j.ces.2005.01.033.
Weller, H.G., Tabor, G., Jasak, H., Fureby, C., 1998. A tensorial approach to computational continuum mechanics using object-oriented techniques. Comput. Phys. 12 (6), 620. https://doi.org/10.1063/1.168744.
Wright, P.R., Glasser, B.J., 2001. Modeling mass transfer and hydrodynamics in fluidized-bed adsorption of proteins. AIChE J. 47 (2), 474–488. https://doi.org/10.1002/aic.690470224.
Wu, Q.C., Zhang, Q.L., Gao, D., Nie, L., Wang, H.B., Yao, S.J., Lin, D.Q., 2018. Mixed-mode expanded-bed adsorption for human serum albumin separation. Ind. Eng. Chem. Res. 57 (3), 1039–1047. https://doi.org/10.1021/acs.iecr.7b03799.
Xia, H.F., Lin, D.Q., Yao, S.J., 2007. Evaluation of new high-density ion exchange adsorbents for expanded bed adsorption chromatography. J. Chromatogr. A 1145 (1–2), 58–66. https://doi.org/10.1016/j.chroma.2006.12.098.
Yang, Z., Sun, Y., 2005. Variations of particle size and bed voidage distributions in expanded bed during transient operation processes. J. Chromatogr. A 1077 (2), 143–150. https://doi.org/10.1016/j.chroma.2005.04.054.
Yun, J., Lin, D.Q., Lu, M.H., Zhong, L.N., Yao, S.J., 2004a. Measurement and modeling of axial distribution of adsorbent particles in expanded bed: taking into account the particle density difference. Chem. Eng. Sci. 59 (24), 5873–5881. https://doi.org/10.1016/j.ces.2004.07.009.
Yun, J., Yao, S.J., Lin, D.Q., Lu, M.H., Zhao, W.T., 2004c. Modeling axial distributions of adsorbent particle size and local voidage in expanded bed. Chem. Eng. Sci. 59 (2), 449–457. https://doi.org/10.1016/j.ces.2003.10.009.
Yun, J., Lin, D.Q., Yao, S.J., 2005. Predictive modeling of protein adsorption along the bed height by taking into account the axial nonuniform liquid dispersion and particle classification in expanded beds. J. Chromatogr. A 1095 (1–2), 16–26. https://doi.org/10.1016/j.chroma.2005.07.120.

Yun, J.X., Lin, D.Q., Yao, S.J., 2004b. Variation of the axial dispersion along the bed height for adsorbents with a density difference and a log-normal size distribution in an expanded bed. Ind. Eng. Chem. Res. 43 (25), 8066–8073. https://doi.org/10.1021/ie049511a.

Zhou, Z.Y., Kuang, S.B., Chu, K.W., Yu, A.B., 2010. Discrete particle simulation of particle–fluid flow: model formulations and their applicability. J. Fluid Mech. 661, 482–510. https://doi.org/10.1017/S002211201000306X.